High Coherence at f and 2 f of Mid-Infrared Supercontinuum Generation in Silicon Germanium Waveguides

Milan Sinobad, Alberto Della Torre, Remi Armand, Barry Luther-Davies, Pan Ma, Stephen Madden, Arnan Mitchell, David Moss, Jean-Michel Hartmann, Jean-Marc Fedeli, et al.

High Coherence at f and $2f$ of Mid-Infrared Supercontinuum Generation in Silicon Germanium Waveguides

Milan Sinobad, Alberto Della Torre, Remi Armand, Barry Luther-Davies, Pan Ma, Stephen Madden, Arnan Mitchell, David J. Moss, Jean-Michel Hartmann, Jean-Marc Fédéli, Christelle Monat, and Christian Grillet

***Abstract*—Absorption spectroscopy based on supercontinuum generation in the mid-infrared is a powerful technique to analyze the chemical composition of samples. Furthermore, phase-coherent supercontinuum sources can enable fast data acquisition with coherent, stable pulses that allow single-shot measurements. We report here a numerical study of the coherence of an octave-spanning mid-infrared supercontinuum source that was experimentally obtained in an air-clad SiGe/Si waveguide. We show that engineering two closely spaced zero-dispersion wavelengths that enclose an anomalous dispersion band centered around a fixed pump wavelength can produce supercontinuum pulses with high spectral density and full coherence at the extreme ends of the spectrum. This work is important for absorption spectroscopy, on-chip optical frequency metrology, and *f*-to-2*f* interferometry applications.**

***Index Terms*—Optical waveguides, silicon germanium, silicon photonics, supercontinuum (SC) generation.**

I. Introduction

Supercontinuum (SC) sources are of great interest because of their high spectral brightness over a large spectral bandwidth. In particular, mid-infrared (mid-IR, 3–20 μm) sources, due to the strong molecular fingerprint in this spectral region [1], are well suited for environmental and toxic vapors sensing in atmospheric, security and industrial applications [2]. Broadband integrated sources can achieve sensing with high throughput thanks to the parallel detection of several species [3]. Their integration in a complementary metal-oxide-semiconductor (CMOS) compatible integrated platform would lead to high volume, low cost sensing technology. Mid-IR SC was first demonstrated in fibers [4]–[7], in a chalcogenide based platform [8] and recently in CMOS compatible platforms [9], [10]. Among the different CMOS compatible platforms that have been proposed for mid-IR SC generation, silicon germanium-on-silicon waveguides are very promising thanks to the wide transparency window up to 8.5 μm [11]–[13] and good nonlinear properties [14]–[16], with the recent demonstration of SC generation from 3 to 8.5 μm [17].

The SC bandwidth is maximal when pumping the nonlinear waveguide structure in the anomalous dispersion regime [18]. For many applications however, a wide bandwidth is not the only requirement. High coherence across the spectrum is also needed. Locking of the fundamental and second harmonic of coherent broadband sources spanning more than one octave (termed f-to-$2f$ self-frequency referencing) has played a major role in the fields of frequency metrology and optical clocks [19]–[21]. Coherent SC sources have also been used for precision spectroscopy, high resolution optical tomography [22], [23] and Raman spectroscopy [24]. In the anomalous dispersion regime, however, the mechanism underlying SC generation is generally dominated by soliton fission triggered by noise-seeded modulation instability leading to shot-to-shot fluctuations and degradation of coherence [18]. To effectively transfer the coherence properties of the pump to the generated SC, several strategies have been used. F. Leo *et al*. demonstrated that coherence could be enforced by a high level of two-photon absorption (TPA). This effectively reduces the soliton number in the waveguide. A high coherence was reported in a 1 cm long silicon-on-insulator waveguide pumped at 1.6 μm with 150 fs pulses [25]. However, this approach typically restricts the SC bandwidth at the output. More frequently, coherence is preserved by using a waveguide only slightly longer than the soliton fission length to alleviate coherence degradation due to modulation instability. Using this approach, A. R. Johnson *et al*. demonstrated coherent SC when pumping silicon-nitride waveguides at 1 μm [26]. Alternatively, extremely short pump pulses can be used, in order to increase the

Manuscript received May 24, 2019; revised August 5, 2019; accepted September 2, 2019. Date of publication September 24, 2019; date of current version October 25, 2019. This work was supported in part by the Agence Nationale de la Recherche (ANR) under Grant ANR-17-CE24-0028 and in part by H2020 European Research Council (ERC) under Grant 648546 GRAPHICS. *(Corresponding author: Milan Sinobad.)*

M. Sinobad, A. D. Torre, R. Armand, C. Monat, and C. Grillet are with Institut des Nanotechnologies de Lyon (INL UMR5270), Université de Lyon 69134 Ecully, France (e-mail: milan.sinobad@ec-lyon.fr; alberto.della-torre@ec-lyon.fr; remi.armand@ec-lyon.fr; christelle.monat@ec-lyon.fr; christian.grillet@ec-lyon.fr).

B. Luther-Davies, P. Ma, and S. Madden are with Laser Physics Centre, Australian National University, Canberra 0100, Australia (e-mail: barry.luther-davies@anu.edu.au; pan.ma@anu.edu.au; stephen.madden@anu.edu.au).

A. Mitchell is with the School of Engineering, RMIT University, Melbourne 3001, Australia (e-mail: arnan.mitchell@rmit.edu.au).

D. J. Moss is with the Centre for Microphotonics, Swinburne University of Technology, Hawthorn 3122, Australia (e-mail: dmoss@swin.edu.au).

J.-M. Hartmann and J.-M. Fédéli are with the CEA-Leti, MINATEC Campus, 38054 Grenoble, France (e-mail: jean-michel.hartmann@cea.fr; jean-marc.fedeli@cea.fr).

Color versions of one or more of the figures in this article are available online at http://ieeexplore.ieee.org.

Digital Object Identifier 10.1109/JSTQE.2019.2943358

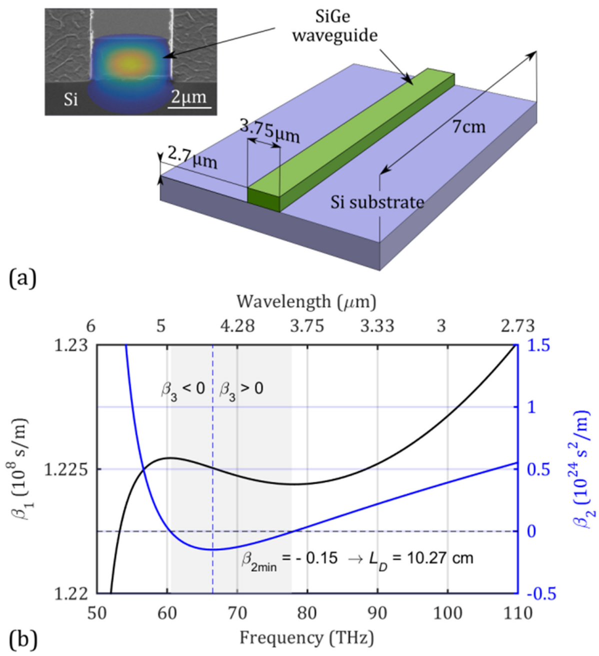

Fig. 1. (a) Waveguide schematics and scanning electron microscope (SEM) image with the superimposed TE fundamental mode electric field profile. (b) β_1 (black, left *y*-scale) and β_2 (blue, right *y*-scale) dispersion curves. The grey area indicates the anomalous dispersion regime. The dispersion length (L_D) is calculated for the minimal value of β_2 represented by the blue dashed vertical line.

soliton fission length. For instance, N. Singh *et al.* generated a SC with a coherence higher than 90%, on average, by pumping a silicon-on-insulator waveguide with sub-100 fs pulses in the short wave infrared (SWIR). This approach is however constraining from the technological point of view [27]. These strategies were recently used to numerically demonstrate high coherence of the supercontinuum in mid-IR generated from the germanium-on-silicon waveguide [28].

Here, we numerically study the coherence properties of a mid-IR supercontinuum (extending from 2.63 to 6.18 μm) that was experimentally generated in a 3.75 μm × 2.70 μm cross-section, 7 cm long silicon germanium-on-silicon ($Si_{0.6}Ge_{0.4}$/Si) waveguide pumped by ~200 fs pulses at $\lambda = 4\ \mu$m [17]. We show that a broad and highly coherent SC can be obtained by pumping the waveguide at a wavelength enclosed in a narrow anomalous dispersion band. Through analysis of the spectrograms and the coherence properties of the SC generated at different locations along the waveguide, we study the dynamics of the underlying mechanism generating the SC in this particular regime. We show that, with this approach, it is possible to achieve a broadband SC with a high degree of coherence irrespectively of the waveguide length and without the need for sub-100 fs pump-pulses or multi-photon absorption.

II. Waveguide Design and Numerical Model

Our device consists of a 7 cm long $Si_{0.6}Ge_{0.4}$ on Si (001) air-clad waveguide with a 3.75 μm × 2.70 μm cross-section [see Fig. 1(a)]. We demonstrated in [17] that by pumping such a waveguide with ~200 fs pulses at 4 μm wavelength,

TABLE I
Numerical Values of the Parameters Used in the Model

Parameter	Value	Dispersion	Value calc. at λ_0 = 4 μm (TE)
λ_0 (μm)	4	β (1/m)	5.5 × 10^{6}
T_{FWHM} (fs)	205	β_1 (s/m)	1.22 × 10^{-8}
P_p (W)	2350	β_2 (s^2/m)	-5.52 × 10^{-26}
		β_3 (s^3/m)	2.46 × 10^{-39}
A_{eff} (μm^2)	6.25	β_4 (s^4/m)	1.94 × 10^{-53}
L (cm)	7	β_5 (s^5/m)	-8.26 × 10^{-68}
α (dB/cm)	0.38	β_6 (s^6/m)	-2.52 × 10^{-81}
n_2 (cm^2/W)	2.55 × 10^{-14}	β_7 (s^7/m)	-1.42 × 10^{-93}
α_{4PA} (cm^5/GW^3)	1.16 × 10^{-6}	β_8 (s^8/m)	1.02 × 10^{-106}
σ (cm^2)	1.45 × 10^{-17} × $(4/1.55)^2$	β_9 (s^9/m)	-2.88 × 10^{-120}
k_c (cm^3)	-5.0 × 10^{-21} × $(4/1.55)^2$	β_{10} (s^{10}/m)	3.16 × 10^{-134}
f_R	0.043		
τ_1 (fs)	12.2		
τ_2 (ps)	3		

we were able to generate high intensity SC signal across a wide bandwidth, with extreme wavelengths (at 2.63 μm and 6.18 μm) separated by an octave. SC is limited by mode cutoff at long wavelengths ($\lambda \sim 6\ \mu$m) which is induced by the asymmetry of the waveguide with respect to the vertical plane. The first and second order dispersions of the waveguide, calculated by a finite-difference mode solver, are shown in Fig. 1(b) as a function of the optical wavelength. The waveguide dispersion thus exhibits two zero-dispersion wavelengths (ZDW) at 3.84 μm and 4.96 μm, respectively, which enclose an anomalous dispersion band highlighted in grey in Fig. 1(b).

The propagation of short optical pulses in a waveguide can be described by the generalized nonlinear Schrodinger equation (GNLSE) under the slowly varying envelope approximation:

$$\frac{\partial A}{\partial z} = -\frac{\alpha}{2}A + \sum i^{m+1}\frac{\beta_m}{m!}\frac{\partial^m A}{\partial t^m} + i\gamma(\omega_0)\left(1 + \frac{i}{\omega}\frac{\partial}{t}\right)A \times \int_{-\infty}^{t} R(t-t')|A|^2 dt' - \frac{\alpha_{4PA}}{2A_{eff}^3}|A|^6 A - \frac{\sigma}{2}(1 - i\mu)N_c A \quad (1)$$

where $A(z, t)$ is the electric field envelope, α is the attenuation coefficient, β_m is the *m*-th order derivative of the propagation constant with respect to the angular frequency, $\gamma(\omega_0)$ is the nonlinear parameter at the central frequency of the pulse, $R(t - t')$ is a function that takes into account Raman contributions, α_{4PA} is the four-photon absorption coefficient, A_{eff} is the effective area at the central frequency of the pulse, N_c is the free-carrier density in the waveguide, σ is the free-carrier absorption cross-section and $\mu = 2k_c k_0/\sigma$ is a dimensionless parameter that encompasses the impact of free-carrier dispersion, with k_0 being the wavenumber and k_c the free-carrier dispersion parameter [16]. High-order dispersions β_m are included up to β_{10} (see Table I). Here, we consider that the propagation loss is constant and equal to 0.38 dB/cm, as measured at 4 μm [17]. The nonlinear Raman response function (*t*) is taken equal to that of crystalline silicon [29]. The fractional contribution of the Raman response to the third-order nonlinearity f_R, the Raman response time τ_1 and the phonon lifetime τ_2 are given in Table I.

The temporal variation of the free-carrier density in the waveguide is modeled by the following rate equation:

$$\frac{\partial N_c}{\partial t} = \frac{\alpha_{4PA}}{4\hbar\omega}\left(\frac{|A|^2}{A_{eff}}\right)^4 \tag{2}$$

The recombination lifetime is neglected in (2), as the reported value in silicon based waveguides (∼10 ns) [30] is (i) much longer than our pulse duration ($T_{\mathrm{FWHM}} = 205$ fs) and (ii) much shorter than the time period between subsequent pulses. The nonlinear parameter and effective area of our waveguide are $\gamma = 0.63$ (W·m)$^{-1}$ and $A_{eff} = 6.25\ \mu\mathrm{m}^2$, respectively [17]. The GNLSE was numerically solved using the split-step Fourier method. The numerical values of the parameters used in the model are summarized in Table I.

The degree of first-order coherence $g^{(1)}{}_{12}$ of the generated supercontinuum is calculated from the following formula [18]:

$$g_{12}^{(1)}(\lambda) = \left|\frac{\langle E_1^*(\lambda)\, E_2(\lambda)\rangle}{\sqrt{\left\langle |E_1(\lambda)|^2\right\rangle \left\langle |E_2(\lambda)|^2\right\rangle}}\right| \tag{3}$$

where the angle brackets denote an ensemble average over forty independently generated pairs of supercontinua $E_{1,2}(\lambda)$ with random input noise. Noise was modelled by adding one photon per mode (according to our pump repetition rate *fr* = 63 MHz) with a Gaussian distribution of both amplitude and phase of variance 2σ equal to $h\nu/2$ and π, respectively [31]. A similar approach has been used to model noise in SC generated in silicon-on-insulator [27] and silicon-on-sapphire platforms [10].

III. Results and Discussion

A. Experimental Supercontinuum Generation and Calculated Coherence

The waveguide was pumped in the Transverse Electrical (TE) polarization by a 200 mW tunable OPA laser (MIROPA-fs, Hotlight Systems) delivering 205 fs pulses centered at 4 μm (75 THz frequency) with a repetition rate of 63 MHz [17].

Fig. 2 (bottom) shows the measured (blue curve) and simulated (black curve) spectra resulting after propagation of a pulse with a 2.35 kW coupled peak power. The experimentally generated SC spans over more than one octave, from 2.63 up to 6.18 μm, with a 3.55 μm bandwidth at −30 dB. The on-chip power spectral density at $\lambda = 5.8\ \mu$m (*f*) is −52 dBm·nm^{-1}. At $\lambda = 2.9\ \mu$m (2*f*), it is greater than −37 dBm·nm^{-1}.

The overall bandwidth of the simulated SC agrees relatively well with that measured experimentally. One striking difference though is that the signals generated by simulations at both *f* and 2*f* exhibit greater power than the average one (−32.6 dBm) calculated over the -30 dB bandwidth. This lower power spectral density on the long wavelength side for the experimental SC is most likely due to water vapor absorption at around 5.5–6 μm [32], which takes place along the free-space path from the chip output to the spectrometer. The lower signal measured at short wavelengths comes from an increase of the measured propagation loss (below $\lambda = 3.5\ \mu$m) that is not considered in our simulations. Fig. 2 (top) shows the calculated coherence, which remains high at the extreme parts of the spectrum. The apparent loss of coherence in the central part of the spectrum, where the signal is lower, is due to the low signal to noise ratio.

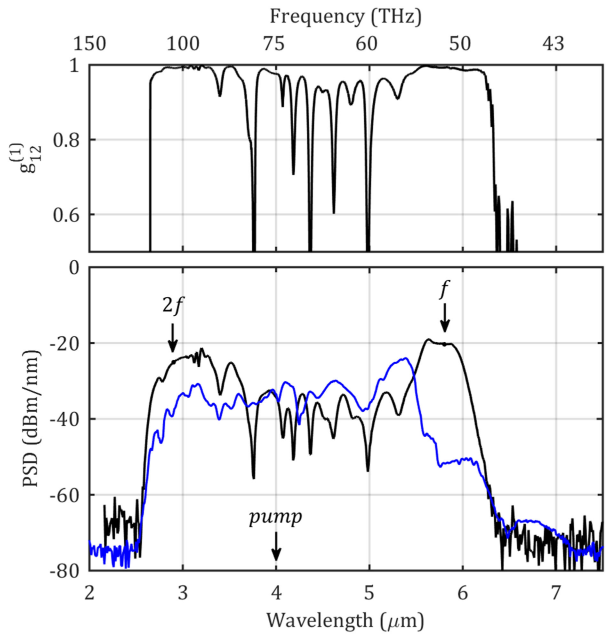

Fig. 2. Calculated coherence at the output of the waveguide (top), experimental (blue) and simulated (black) spectra (bottom) for $\lambda_p = 4\ \mu$m, $T_{\mathrm{FWHM}} = 205$ fs and $P_p = 2.35$ kW. The spectrum is simulated with added noise, i.e one photon per mode with random phase and amplitude.

Fig. 3 shows the evolution of the pulse, as calculated from simulations, in the time domain (a), the spectrum (b) and the coherence (c) as a function of the propagation distance up to 7 cm.

After a few centimeters of propagation along the waveguide, the central part of the spectrum, close to the pump wavelength appears to be depleted relative to the normal dispersion bands towards the high and low wavelengths [Fig. 3(b)]. Full coherence is achieved at the extreme parts of the SC spectrum at all propagation distances [Fig. 3(c)]. Moreover, by choosing the waveguide length slightly shorter (∼2 cm), it is possible to maintain high coherence across the entire spectrum without affecting the spectral bandwidth, as the spectrum is already fully broadened [see red line in Fig. 3(c)]. In contrast to the strategies that have been pursued in references [25], [27], the coherence is not degraded here by the use of a pump pulse duration longer than 100 fs nor by the low multi-photon absorption. Finally, we do not observe on Fig. 3(a) the temporal pulse compression that typically governs the dynamics of SC in the anomalous dispersion regime and leads to soliton fission. We investigate the origin of these features in the next section.

B. Supercontinuum Generation Dynamics

In this section, we numerically investigate the dynamics of SC generation in our waveguide pumped in an anomalous dispersion

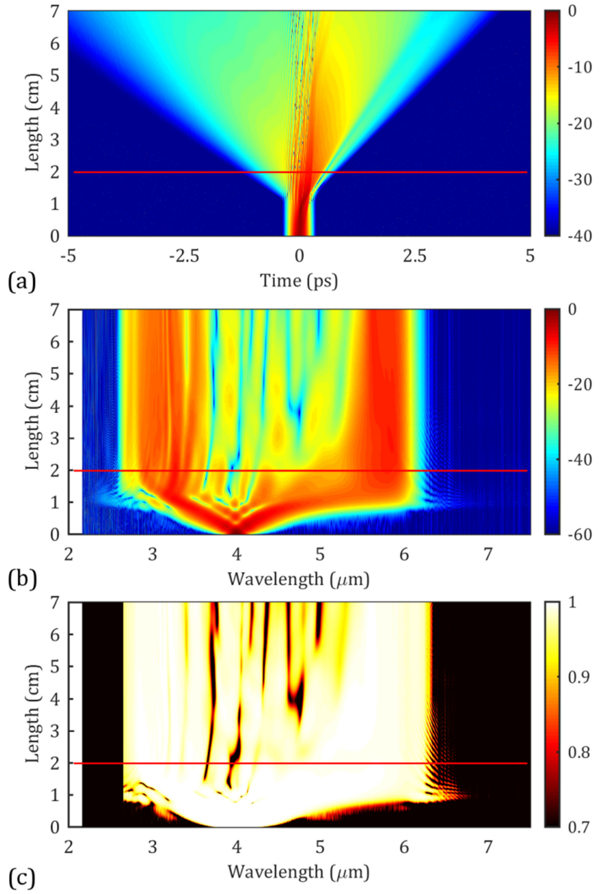

Fig. 3. Evolution of the simulated pulse in the (a) time domain, (b) spectrum, and (c) coherence at different propagation distances for $\lambda_p = 4\,\mu$m, $T_{\mathrm{FWHM}} = 205$ fs, and $P_p = 2.35$ kW.

band surrounded by two closely spaced ZDWs (here, at 3.84 and 4.96 μm). The dynamics of SC generation when pumping in a narrow anomalous dispersion band has been explored in optical fibers [33]–[35]. Different explanations have been raised, discussing the interplay of self-phase modulation (SPM) and four-wave mixing (FWM) as well as the formation of solitons, soliton annihilation and the generation of dispersive waves. The bandwidth of the central anomalous dispersion window with respect to the pump characteristics critically governs the mechanisms that drive the SC dynamics. Furthermore, although the potential for pulse recompression was numerically shown in [33], none of these papers explicitly studied the coherence properties of the spectra.

To get more insights into the underlying phenomena that dominate the generation of our mid-IR SC, we simulate the pulse evolution in both the spectral and time-domain at intermediate distances along our waveguide length. Considering our waveguide dispersion and pump characteristics, the soliton fission length given by $L_{fiss} = T_0/(\gamma P_0|\beta_2|)^{1/2}$ is equal to $L_{fiss} = 1.38$ cm and the input soliton order is $N = 20$. Fig. 4 shows the spectrum, time-domain and spectrogram of the SC signal generated at 8 intermediate steps along the 7 cm long waveguide due to a pump pulse with a peak power equal to 2.35 kW at 4 μm (75 THz frequency). The spectrogram provides simultaneous information about the temporal and spectral profile

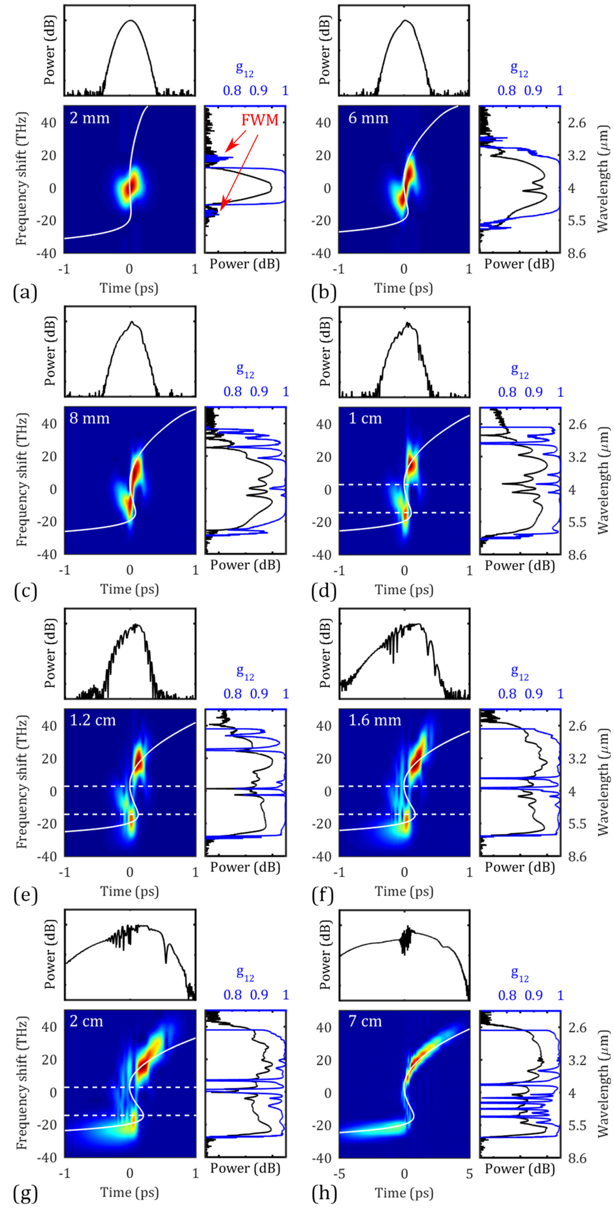

Fig. 4. Calculated spectrogram with superimposed group delay (white curve), pulse in time domain, spectrum (black curve) and coherence (blue curve) at (a) 2 mm, (b) 6 mm, (c) 8 mm, (d) 1 cm, (e) 1.2 cm, (f) 1.6 cm, (g) 2 cm and (h) 7 cm length. The frequency shift is calculated with respect to the input pump frequency (75 THz). The white dashed lines in (d) to (g) present the boundaries of the anomalous dispersion band.

of the pulse, and its related chirp. It is mathematically described as:

$$\Sigma(\omega, \tau) = \left| \int_{-\infty}^{\infty} E(t)\, g(t-\tau)\, e^{-i\omega t} dt \right|^2 \qquad (4)$$

with $g(t-\tau)$ being a variable-delay Gaussian shape gate function with $\sim$130 fs duration [18].

Up to 0.6 cm distance propagation, the spectrum shows the typical features of SPM, with 3 lobes that are roughly symmetric around the pump wavelength and a positive linear chirp [see Fig. 4(b)]. The effect of dispersion in the vicinity of the pump wavelength is indeed negligible after this short distance ($L_D = 27.6$ cm for our 205 fs pulses). This is indicated by the

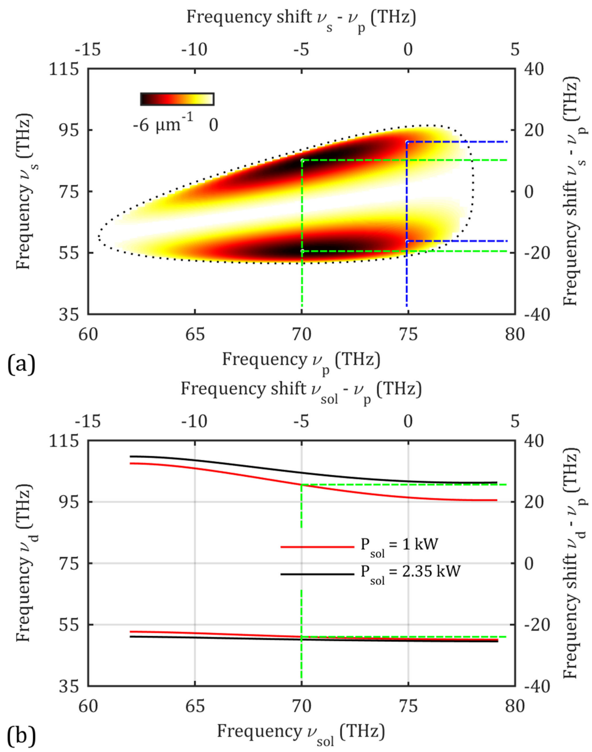

Fig. 5. (a) Linear phase mismatch for degenerate four-wave mixing around the pump frequency v_p. The black dotted line represents the frequencies corresponding to a zero linear phase mismatch. The dashed blue and green lines point out the frequencies with the maximum negative phase mismatch for a pump at 75 and 70 THz frequency (v_p) respectively. (b) Phase matched frequencies to a soliton of frequency varied across the anomalous dispersion band for 1 kW (red) and 2.35 kW (black) of soliton peak power. The dashed green lines point out the frequencies that are phase matched to a soliton of 1 kW peak power at 70 THz.

group delay, close to zero around the pump, represented by the white solid curve superimposed to the spectrogram. At the same time, some signal appears from noise in frequency bands at ± 16 THz from the input frequency, corresponding to 3.3 and 5.1 μm wavelengths [see Fig. 4(a) and (b)].

To better clarify the origin of these sidebands, we calculated the spectral dependence of the linear phase mismatch associated with degenerate four-wave mixing (FWM) pumped at the angular frequency ω_p and given by the following equation [36], [37]:

$$\Delta\beta = 2\beta(\omega_p) - \beta(\omega_s) - \beta(\omega_i) \quad (5)$$

where ω_s and ω_i are the angular frequencies of the signal and the idler respectively. The result associated with our waveguide dispersion is plotted on Fig. 5(a) as a function of the FWM pump frequency ν_p (bottom axis), and the frequency shift (top axis) with respect to the 75 THz (input) frequency. For $\nu_p = 75$ THz, this curve exhibits two minimum (negative) linear phase mismatch values equal to -3.4 cm^{-1}. They are reached for symmetric frequencies ν_s at ± 16 THz from the 75 THz pump (blue dashed line). The value of the nonlinear phase mismatch $2\gamma P_p$, which counterbalances the linear one, is equal to 15 cm^{-1} close to the entrance of the waveguide. Hence, the spontaneous generation of a probe and an idler signal by degenerate FWM of the pump signal will be more effective at the two frequencies (± 16 THz), for which the total (linear and nonlinear) phase mismatch is closer to zero. We therefore attribute the symmetrically positioned side bands observed in the SC spectrum close to the entrance of the waveguide to noise seeded spontaneous FWM. As expected, this signal is not fully coherent ($g_{12} < 0.8$) [see blue curve in Fig. 4(a)] and exhibits a relatively broad bandwidth.

Between 0.8 cm and 1.2 cm along the waveguide length, dispersion starts being substantial (see the negative group delay presented with white curve in Fig. 4(c) and (d) around the pump wavelength). Yet, due to continued SPM and the limited bandwidth of the central anomalous dispersion window, a significant amount of power has been already pushed outside of the anomalous dispersion band [see Fig. 4(d) and (e)]. The depletion of the anomalous dispersion region results in an apparent loss of coherence in the central part of the spectrum, which is however only a consequence of the low signal to noise ratio. From the spectrograms, two high energy pulses appear and split in the spectral (and time-) domain, lying very close to the two ZDWs. The pulse on the low wavelength trailing edge, in particular, strongly overlaps with the normal dispersion regime ($L = 1$ and 1.2 cm) and seems to undergo some SPM on its own with a positive linear chirp growing between 1.2 and 2 cm, generating, in turn, more side lobes in this part of the spectrum. These new components generated by SPM in a normal dispersion regime are highly coherent, as seen in Fig. 4(f)–(g).

At around 1 cm, some part of the pump energy, which is redshifted by around -5 THz from the input frequency, remains in the middle of the anomalous dispersion band. Subsequent transfer of energy occurs from this band to both sides of the spectrum [Fig. 4(e)–(g)]. The oscillations occurring in the temporal domain at the leading edge of the pulse [for $L = 1.2$ and 1.6 cm in Fig. 4(e) and (f)], having a period of $\sim$50 fs, can be seen as the result of the beating between frequencies with a 20 THz distance. At the low level, the observed energy transfer might be attributed to degenerate FWM between the remaining redshifted signal in the anomalous dispersion band (which could act as a pump) and the tail of the low energy peak at ~ -20 THz (which could act as an idler), leading to the generation of a signal at higher frequencies and to an enhancement of the idler [38]. This interpretation roughly agrees with the frequencies at which the calculated FWM linear phase mismatch is minimum [Fig. 5(a), green dashed lines]. For a pump at 70 THz (i.e., -5 THz from the input frequency), these correspond to an idler at around -20 THz and a signal at around 10 THz from the input frequency. Indeed, the estimated nonlinear phase mismatch induced by the pump signal in the anomalous band (estimation 6 cm^{-1}) compensates for the maximum negative linear phase mismatch values afforded by the waveguide dispersion (-6 cm^{-1}), leading to more effective FWM at frequencies corresponding to the minimum (negative) linear phase mismatch.

As an alternative interpretation, the energy transfer around the two ZDWs between 1 cm and 2 cm could be understood as dispersive wave generation seeded by a soliton at -5 THz. The corresponding phase matching condition is given by the following equation [37]:

$$\beta\left(\omega_{sol}\right)+\beta_1\left(\omega_{sol}\right)\left(\omega_d-\omega_{sol}\right)+\frac{1}{2}\gamma P_{sol}-\beta\left(\omega_d\right)=0 \quad (6)$$

where ω_d and ω_{sol} are the dispersive wave and soliton angular frequencies, respectively, and P_{sol} is the soliton peak power. Fig. 5(b) plots the frequencies that are phase matched with the soliton as a function of its frequency. As a rough approximation, this calculation considers that the duration of the soliton is that of the pump ($T_{\mathrm{FWHM}} = 205$ fs) and that its peak power is either 1 kW or 2.35 kW. The 1 kW peak power would correspond to a soliton carrying 40% of the input pulse power [estimated from the spectrogram on Fig. 4(d)] which would not experience pulse compression. In this case, dispersive waves are expected to be generated at around -24 and $+25$ THz from the input frequency (i.e., about -20 and $+30$ THz from the redshifted signal in the anomalous band). It is difficult to unambiguously attribute the redshifted signal at -5 THz to a soliton. However, this dispersive wave mechanism could explain part of the signal that is transferred spectrally further from the pump than the aforementioned FWM mechanism at 1.6 and 2 cm [Fig. 4(f)–(g)]. In addition, the $\sim$50 fs time-domain oscillation at the leading edge of the pulse could be explained by the beating between the -5 THz red-shifted signal and the low energy (-24 THz) dispersive wave.

Considering the relatively broad generated features in the spectrum though, we cannot rule out either of the two mechanisms. We note that the high frequency band is slightly broader, which might be due to the distinct frequencies that are created in this range by each process (10 THz and 25 THz for FWM and dispersive wave, respectively). We therefore conclude that the observed spectrum is most likely the result of the interplay between SPM, FWM and dispersive wave generation. Most importantly, all these processes preserve coherence.

At 2 cm [Fig. 4(g)], following this energy transfer, the two sidebands in the normal regime carry most of the power. Further propagation [Fig. 4(h)] results in the attenuation of the pulse around the pump wavelength due to linear and nonlinear loss and in the temporal separation of the two side bands according to the distinct group delay in these two bands (see white group delay curve in Fig. 4)

From this analysis, we can understand the high degree of coherence obtained for our supercontinuum. Its generation is dominated by mechanisms that all preserve coherence, namely SPM and energy transfer through FWM and/or dispersive wave generation. We stress that, due to the high amount of energy pushed out of the anomalous dispersion window in the early stages of the propagation, the effective soliton number is probably less than 20, therefore limiting the detrimental impact of soliton fission on coherence. As a result of its limited bandwidth, the anomalous dispersion band cannot accommodate the entire spectrally broadened spectrum before soliton fission occurs. We thus do not observe the typical temporal pulse compression leading to soliton fission nor clear evidence of soliton fission in the time domain. Finally, we note that although the absolute bandwidth of the anomalous dispersion region is relatively wide in our case, i.e., 1160 nm compared to 165 nm in [33], the bandwidth to pump wavelength ratio is comparable, as we pump in the mid-IR region. We thus observe a similar dynamics to that observed for fibers with a narrow anomalous dispersion band in the near-IR [33]. This leads to high coherence over most of the spectrum, in particular at frequencies distanced by one octave.

The high power spectral density and high degree of coherence at the extreme parts of the octave spanning SC makes this spectrum particularly interesting for *f*-to-2*f* interferometry [39]. A *f*-to-2*f* interferometer based technique has been proposed in 1999 by H. R. Telle *et al.* [19] to measure and stabilize the carrier-envelope offset of two-cycle lasers, a fundamental requirement for high-harmonic generation applications [40]. Moreover, measuring the radio-frequency beats that can be generated via *f*-to-2*f* self-frequency referencing using broadband laser sources spanning over one octave can be used to stabilize pulse for high precision spectroscopy and frequency metrology applications. The coherence of dispersive waves at *f* and 2*f* is not affected by the low multi-photon absorption, allowing us to take full advantage of the extremely low nonlinear losses to maximize SC bandwidth and output power. Furthermore, the generated SC covers a great part of the molecular fingerprint region, with potential applications for on-chip spectroscopy.

IV. Conclusion

We have shown that an on-chip mid-IR octave spanning supercontinuum generated in an anomalous dispersion regime surrounded by two closely spaced ZDWs maintained a high degree of coherence at its extreme parts. The interplay between the different mechanisms driven by this specific dispersion profile ensures that coherence is achieved without requiring high TPA, specific waveguide length, nor being constrained by the use of sub-100 fs input pulses. Since the spectrum covers the molecular fingerprint region, the reported SC is well suited for on-chip sensing applications. Moreover, the high power spectral density and the high coherence of the octave-distanced signals make this supercontinuum source promising for *f*-to-2*f* interferometry, with potential applications for high-precision spectroscopy and frequency metrology.

Acknowledgment

We acknowledge the support of the International Associated Laboratory between France and Australia (LIA ALPhFA), and author Christelle Monat acknowledges the support of the Institut Universitaire de France.

References

[1] Y.-C. Chang, *Design, Fabrication and Characterization of Mid-Infrared Strip Waveguide for Laser Spectroscopy in Liquid Environments*. Lausanne, Switzerland: EPFL, 2012.

[2] A. Schliesser, N. Picqué, and T. W. Hänsch, “Mid-infrared frequency combs,” *Nature Photon.*, vol. 6, pp. 440–449, 2012.

[3] H. Pires, M. Baudisch, D. Sanchez, M. Hemmer, and J. Biegert, “Ultrashort pulse generation in the mid-IR,” *Prog. Quant. Electron.*, vol. 43, pp. 1–30, 2015.

[4] Y. Yu *et al.*, “1.8–10 μm mid-infrared supercontinuum generated in a step-index chalcogenide fiber using low peak pump power,” *Opt. Lett.*, vol. 40, pp. 1081–4, Mar. 2015.

[5] T. Cheng *et al.*, "Mid-infrared supercontinuum generation spanning 2.0 to 15.1 μm in a chalcogenide step-index fiber," *Opt. Lett.*, vol. 41, pp. 2117–20, May 2016.
[6] C. R. Petersen *et al.*, "Increased mid-infrared supercontinuum bandwidth and average power by tapering large-mode-area chalcogenide photonic crystal fibers," *Opt. Express*, vol. 25, pp. 15336–15348, Jun. 2017.
[7] D. D. Hudson *et al.*, "Toward all-fiber supercontinuum spanning the mid-infrared," *Optica*, vol. 4, p. 1163, 2017.
[8] Y. Yu *et al.*, "Experimental demonstration of linearly polarized 2–10 μm supercontinuum generation in a chalcogenide rib waveguide," *Opt. Lett.*, vol. 41, pp. 958–61, Mar. 2016.
[9] N. Singh *et al.*, "Midinfrared supercontinuum generation from 2 to 6 μm in a silicon nanowire," *Optica*, vol. 2, pp. 797–802, 2015.
[10] N. Nader *et al.*, "Versatile silicon-waveguide supercontinuum for coherent mid-infrared spectroscopy," *APL Photon.*, vol. 3, 2018, Art. no. 036102.
[11] R. Soref, "Mid-infrared photonics in silicon and germanium," *Nature Photon.*, vol. 4, pp. 495–497, 2010.
[12] J. M. Ramirez *et al.*, "Low-loss Ge-rich Si0.2Ge0.8 waveguides for mid-infrared photonics," *Opt. Lett.*, vol. 42, pp. 105–108, Jan. 2017.
[13] J. M. Ramirez *et al.*, "Graded SiGe waveguides with broadband low-loss propagation in the mid infrared," *Opt. Express*, vol. 26, pp. 870–877, Jan. 2018.
[14] N. K. Hon, R. Soref, and B. Jalali, "The third-order nonlinear optical coefficients of Si, Ge, and $Si_{1-x}Ge_x$ in the midwave and longwave infrared," *J. Appl. Phys.*, vol. 110, pp. 11301–11301, 2011.
[15] L. Carletti *et al.*, "Nonlinear optical response of low loss silicon germanium waveguides in the mid-infrared," *Opt. Express*, vol. 23, pp. 8261–71, Apr. 2015.
[16] L. Carletti *et al.*, "Mid-infrared nonlinear optical response of Si-Ge waveguides with ultra-short optical pulses," *Opt. Express*, vol. 23, pp. 32202–14, Dec. 2015.
[17] M. Sinobad *et al.*, "Mid-infrared octave spanning supercontinuum generation to 8.5 μm in silicon-germanium waveguides," *Optica*, vol. 5, pp. 360–366, Apr. 2018.
[18] J. M. Dudley, G. Genty, and S. Coen, "Supercontinuum generation in photonic crystal fiber," *Rev. Mod. Phys.*, vol. 78, pp. 1135–1184, Apr. 2006.
[19] H. R. Telle *et al.*, "Carrier-envelope offset phase control: A novel concept for absolute optical frequency measurement and ultrashort pulse generation," *Appl. Phys. B*, vol. 69, pp. 327–332, 1999.
[20] R. Holzwarth *et al.*, "Optical frequency synthesizer for precision spectroscopy," *Phys. Rev. Lett.*, vol. 85, p. 2264, 2000.
[21] T. Udem, R. Holzwarth, and T. W. Hänsch, "Optical frequency metrology," *Nature*, vol. 416, p. 233, Mar. 2002.
[22] I. Hartl *et al.*, "Ultrahigh-resolution optical coherence tomography using continuum generation in an air-silica microstructure optical fiber," *Opt. Lett.*, vol. 26, pp. 608–610, 2001.
[23] N. Nishizawa, Y. Chen, P. Hsiung, E. Ippen, and J. Fujimoto, "Real-time, ultrahigh-resolution, optical coherence tomography with an all-fiber, femtosecond fiber laser continuum at 1.5 μm," *Opt. Lett.*, vol. 4, pp. 2846–2848, 2004.
[24] H. Kano and H.-O. Hamaguchi, "Characterization of a supercontinuum generated from a photonic crystal fiber and its application to coherent Raman spectroscopy," *Opt. Lett.*, vol. 28, pp. 2360–2362, 2003.
[25] F. Leo, S. P. Gorza, S. Coen, B. Kuyken, and G. Roelkens, "Coherent supercontinuum generation in a silicon photonic wire in the telecommunication wavelength range," *Opt. Lett.*, vol. 40, pp. 123–6, Jan. 2015.
[26] A. R. Johnson *et al.*, "Octave-spanning coherent supercontinuum generation in a silicon nitride waveguide," *Opt. Lett.*, vol. 40, pp. 5117–20, Nov. 2015.
[27] N. Singh *et al.*, "Octave-spanning coherent supercontinuum generation in silicon on insulator from 1.06 μm to beyond 2.4 μm," *Light Sci. Appl.*, vol. 7, pp. 17131–17138, 2018.
[28] J. Yuan *et al.*, "Mid-infrared octave-spanning supercontinuum and frequency comb generation in a suspended Germanium-membrane ridge waveguide," *J. Lightw. Technol.*, vol. 35, pp. 2994–3002, Jul. 2017.
[29] L. A. L. Yin, Q. Lin, and G. P. Agrawal, "Soliton fission and supercontinuum generation in silicon waveguides.," *Opt. Lett.*, vol. 32, pp. 391–393, 2007.
[30] Q. Lin, O. J. Painter, and G. P. Agrawal, "Nonlinear optical phenomena in silicon waveguides: Modeling and applications," *Opt. Express*, vol. 15, pp. 16604–16644, Dec. 2007.
[31] A. Ruehl *et al.*, "Ultrabroadband coherent supercontinuum frequency comb," *Phys. Rev. A*, vol. 84, Jul. 2011, Art. no. 011806.
[32] P. Linstrom, *NIST Chemistry WebBook*, NIST Standard Reference Database 69, Boulder, CO, USA: NIST, 1997.
[33] K. M. Hilligsøe *et al.*, "Supercontinuum generation in a photonic crystal fiber with two zero dispersion wavelengths," *Opt. Express*, vol. 12, pp. 1045–1054, 2004.
[34] M. H. Frosz, P. Falk, and O. Bang, "The role of the second zero-dispersion wavelength in generation of supercontinua and bright-bright soliton-pairs across the zero-dispersion wavelength," *Opt. Express*, vol. 13, pp. 6181–6192, 2005.
[35] I. Babushkin *et al.*, "Simple route toward efficient frequency conversion for generation of fully coherent supercontinua in the mid-IR and UV range," *Light Sci. Appl.*, vol. 6, p. e16218, Feb. 2017.
[36] M. R. Lamont, B. T. Kuhlmey, and M. C. de Sterke, "Multi-order dispersion engineering for optimal four-wave mixing," *Opt. Express*, vol. 16, pp. 7551–7563, Mar. 2008.
[37] G. P. Agrawal, *Nonlinear Fiber Optics*, 5th ed. Amsterdam, The Netherlands: Academic Press, 2012.
[38] D. Castello-Lurbe, N. Vermeulen, and E. Silvestre, "Towards an analytical framework for tailoring supercontinuum generation," *Opt. Express*, vol. 24, pp. 26629–26645, Nov. 2016.
[39] M. Yu, B. Desiatov, Y. Okawachi, A. L. Gaeta, and M. Lončar, "Coherent two-octave-spanning supercontinuum generation in lithium-niobate waveguides," *Opt. Lett.*, vol. 44, pp. 1222–1225, Mar. 2019.
[40] A. de Bohan, P. Antoine, D. B. Milošević, and B. Piraux, "Phase-dependent harmonic emission with ultrashort laser pulses," *Phys. Rev. Lett.*, vol. 81, p. 1837, 1998.

Milan Sinobad received the B.Sc. degree in electrical engineering from Belgrade University, Serbia, in 2012, and the M.Sc. degree in nanoscale engineering from the Université de Lyon, France, in 2014. He is currently working toward the Ph.D. degree in engineering with the RMIT University, Melbourne, Australia.

His research interests include silicon photonics, mid-infrared photonics, laser physics, and nonlinear optics.

Alberto Della Torre received the B.Sc. degree in engineering physics from the Polytechnic of Milan, in 2015, and the M.Sc. degree in nanoscale engineering from the Université de Lyon, Lyon, France, in 2017. Currently, he is working toward the Ph.D. degree in engineering with the Institut des Nanotechnologies de Lyon (INL), Ecole Centrale de Lyon, Ecully, France.

His research interests include nonlinear optics, mid-infrared photonics, silicon photonics, and photonic crystals.

Remi Armand received the B.S. degree in electrical engineering from the Ecole Normal Supérieur de Cachan, Cachan, France, in 2015, and the M.S. degree in electrical engineering from the Université Paris-Saclay, Saclay, France, in 2018. He is currently working toward the Ph.D. degree in physics with the Ecole Centrale de Lyon, Ecully, France.

His research interests include the design of structure to generate mid-infrared broadbrand sources, and fundamental study of nonlinear photonics.

Barry Luther-Davies received the B.Sc. and Ph.D. degrees in laser physics and nonlinear optics from the University of Southampton, Southampton, U.K., in 1970 and 1974, respectively.

He is an Emeritus Professor of laser physics with the Australian National University (ANU), Canberra, Australia, with experience in the diverse areas of research including lasers, laser–matter interaction physics, photonics, optical materials, and nonlinear optics. He joined the ANU in 1974, where he led a team working on the physics of laser-produced plasmas, until the early 1990s, when the research evolved into studies of laser-materials processing and pulsed laser deposition of thin films. More recently, he has specialized in nonlinear optical materials and devices and photonics with a strong interest in the development of devices for optical signal processing as part of the Australian Research Council's Centre of Excellence for Ultrahigh-Bandwidth Devices for Optical Systems (CUDOS). He has published more than 300 papers in scientific journals, contributed several book chapters and many hundreds of conference papers.

Dr. Luther-Davies is a Fellow of the Optical Society of America and the Australian Academy for Technological Sciences and Engineering. He was awarded the Pawsey Medal of the Australian Academy of Science in 1986 for his contribution to laser–plasma interaction physics and was an ARC Federation Fellow from 2003 to 2008. He serves as an Advisory Editor for Optics Communications.

Pan Ma, photograph and biography not available at the time of publication.

Stephen J. Madden received the B.Sc. degree in electronic engineering and the Ph.D degree in integrated optics from Imperial College in London, London, U.K., in 1985 and 1989, respectively.

He is Associate Professor and a Fellow with Laser Physics Centre, Australian National University (ANU), Canberra, Australia. He has spent most of his career in industry. In 1991, he joined the Telstra Research Laboratories, Melbourne, Australia. In 1997, he became the Director of Research at ADC Telecommunications, Minneapolis, MN, USA, before leaving to become VP engineer with the Sparkolor Corporation, Santa Clara, CA, USA, in 2001. More recently, he led a research within CUDOS, a research consortium between seven Australian universities, into photonics devices. He has published more than 200 papers.

Arnan Mitchell received the Ph.D. degree in engineering from RMIT University, Melbourne VIC, Australia, in 2000.

He is a Distinguished Professor with the School of Engineering, RMIT University, Bundoora, Australia, and is Director of RMIT Micro Nano Research Facility. He is a highly multidisciplinary researcher working in microchip technologies combining light, sound, fluids, and electronics with applications spanning radar systems for defence, high-speed fiber-optic communications, and point-of-care diagnostic systems for biomedicine. He is enthusiastic about translating technology into the hands of end-users and has dedicated much of his career to building diverse teams and comprehensive micro and nanotechnology infrastructure to enable breakthrough discoveries to achieve real-world impact.

David J. Moss (S'83–M'88–SM'09–F'16) received the B.Sc. degree in physics from the University of Waterloo, Waterloo, ON, Canada, and the M.Sc. and Ph.D. degrees in nonlinear optics from the University of Toronto, Toronto, ON, in 1983 and 1988, respectively.

He is the Director of the Centre for Micro-Photonics with the Swinburne University of Technology, Melbourne, Australia, leading research programs in integrated nonlinear nanophotonics, microwave photonics, telecommunications, quantum optics, biophotonics, renewable energy, and other areas. From 1988 to 1992, he was with the National Research Council of Canada, Institute for Microstructural Sciences, Ottawa, Canada, working on III–V optoelectronic devices. From 1992 to 1994, he was a Senior Visiting Scientist with the Hitachi Central Research Laboratories, Tokyo, Japan, working on high-speed optoelectronic devices for 10-Gb/s fiber-optic telecommunications systems. From 1994 to 1998, he was a Senior Research Fellow with the Optical Fiber Technology Centre, University of Sydney, Australia. From 1998 to 2003, he was a Manager with JDS Uniphase, Ottawa, Canada, leading a team developing products for 40-Gb/s telecommunications systems. From 2003 to 2013, he was with the University of Sydney and the Centre for Ultra-High Bandwidth Devices for Optical Systems working on ultrahigh bandwidth optical signal processing, integrated nonlinear nanophotonic circuits, and photonic crystal devices. He has about 600 journal/conference papers including a *Nature*, *Science*, eight *Nature Photonics*, and five *Nature Communications* papers.

Dr. Moss received the 2011 Australian Museum Eureka Science Prize and the Google Australia Award for innovation in computer science. He has been active on many conference committees, including the General Program Chair of OSA Integrated Photonics Research in Vancouver, July 2016, and the General Chair in New Orleans, 2017. He is a Fellow of the IEEE Photonics Society, the Fellow of the Optical Society of America, and the SPIE.

Jean-Michel Hartmann received the Ph.D. degree in physics from Université Grenoble Alpes, France, in 1997.

He joined CEA, Leti, Grenoble, France, in 1999, as a SiGeC Epitaxy Research Scientist. He was a Postdoctoral Fellow with the Imperial College, London, U.K. He is currently coordinating group-IV epitaxy activities in Leti's Technological PlatForm Department. He has the rank of CEA Research Director.

Jean-Marc Fédéli received the Electronics Engineer Diploma from INPG Grenoble, Grenoble, France, in 1978.

He was involved in the development of various magnetic memories and magnetic components as Project Leader, Group Leader, and Program Manager with the CEA-LETI, Grenoble, France. For two years, he was Advanced Program Director with the Memscap Company, France, for the development of RF-MEMS, then with the CEA-LETI in 2002 as a Coordinator of silicon photonic projects until 2012. Under a larger research partnership, he works on many technological aspects on photonics on CMOS (Si rib and stripe waveguides, a-Si waveguides, slot waveguides), Si modulators, Ge photodetectors, and InP integrated sources on Si. He has been participating in different European projects such as EPIXFAB for MPW circuit fabrication and has coordinated the FP7 PLAT4M project on Silicon Photonics Platform. Since 2014, he has moved to sensing activities with photonics, and he is currently the Technical Manager of the H2020 MIRPHAB pilot line on liquid and gas systems sensors. His H factor is around 35 with more than 200 publications and 50 patents. He is the author of three book chapters (one on magnetic recording and two on silicon photonics).

Christelle Monat (M'08) received the Ph.D. degree in electronic integrated devices from the Ecole Centrale de Lyon, Ecully, France, in 2003.

She was with the École Polytechnique Fédérale de Lausanne, Switzerland, for two years, where she was involved in research on single-photon sources. She joined the Centre for Ultrahigh-bandwidth Devices for Optical Systems (CUDOS), School of Physics, University of Sydney, Australia, in late 2005 and led the research on slow light-enhanced nonlinear optics between 2007 and 2010. Since late 2010, she has been an Associate Professor with the Institut des Nanotechnologies de Lyon, Ecole Centrale de Lyon, and was awarded an ERC consolidator grant on graphene-based nonlinear photonic integrated circuits in 2015. Her current research interests include slow light, photonic crystals, III–V Si hybrid photonics, microlasers, and nonlinear optics in the near- and mid-IR.

Christian Grillet received the Ph.D. degree in electronic integrated devices from the Ecole Centrale de Lyon, Ecully, France, in 2003.

In 2004, he joined the Centre for Ultrahigh-bandwidth Devices for Optical Systems (CUDOS), University of Sydney, Sydney, Australia. He then joined Centre national de la recherche scientifique (CNRS), Paris, France, in 2013. He leads the International Associated Laboratory in Photonics between France and Australia (LIA ALPhFA). His research interests include integrated nonlinear optics, mid-infrared integrated optics, photonic crystals, and slow light.